Pure Appl. Geophys.

DOI 10.1007/s00024-014-0988-3

Pure and Applied Geophysics

Advanced Tsunami Numerical Simulations and Energy Considerations by use of 3D–2D Coupled Models: The October 11, 1918, Mona Passage Tsunami

Alberto M. López-Venegas,[1] Juan Horrillo,[2] Alyssa Pampell-Manis,[2]
Victor Huérfano,[1] and Aurelio Mercado[3]

Abstract—The most recent tsunami observed along the coast of the island of Puerto Rico occurred on October 11, 1918, after a magnitude 7.2 earthquake in the Mona Passage. The earthquake was responsible for initiating a tsunami that mostly affected the northwestern coast of the island. Runup values from a post-tsunami survey indicated the waves reached up to 6 m. A controversy regarding the source of the tsunami has resulted in several numerical simulations involving either fault rupture or a submarine landslide as the most probable cause of the tsunami. Here we follow up on previous simulations of the tsunami from a submarine landslide source off the western coast of Puerto Rico as initiated by the earthquake. Improvements on our previous study include: (1) higher-resolution bathymetry; (2) a 3D–2D coupled numerical model specifically developed for the tsunami; (3) use of the non-hydrostatic numerical model NEOWAVE (non-hydrostatic evolution of ocean WAVE) featuring two-way nesting capabilities; and (4) comprehensive energy analysis to determine the time of full tsunami wave development. The three-dimensional Navier–Stokes model tsunami solution using the Navier–Stokes algorithm with multiple interfaces for two fluids (water and landslide) was used to determine the initial wave characteristic generated by the submarine landslide. Use of NEOWAVE enabled us to solve for coastal inundation, wave propagation, and detailed runup. Our results were in agreement with previous work in which a submarine landslide is favored as the most probable source of the tsunami, and improvement in the resolution of the bathymetry yielded inundation of the coastal areas that compare well with values from a post-tsunami survey. Our unique energy analysis indicates that most of the wave energy is isolated in the wave generation region, particularly at depths near the landslide, and once the initial wave propagates from the generation region its energy begins to stabilize.

Key words: 1918 Mona, tsunami, submarine landslide, volume of fluid, three-dimensional model, non-hydrostatic model, tsunami energy.

1. Introduction

The most recent tsunami affecting the island of Puerto Rico in the northeastern Caribbean occurred on October 11, 1918. The tsunami, which affected mostly the northwest coast of the island, was observed shortly after a M_w (Doser *et al.* 2005) earthquake originating somewhere in the Mona Passage (Fig. 1). A post-tsunami survey carried out by Reid and Taber (1919) reported runups ranging from 3 to 8 m along the northwest coast of Puerto Rico, approximately four million dollars in damage, 110 casualties from the earthquake destruction, and 40 people drowned as a result of the tsunami.

The first attempt to model the October 11, 1918, tsunami was that of Mercado and McCann (1998), who assumed an instantaneous co-seismic dislocation as the initial tsunami source. Although their fault model yielded overall good agreement, it was unable to reproduce the observed negative polarity of the first wave arrival and detailed runups. An alternative mechanism for this tsunami was based on the assumption that the earthquake initiated a submarine landslide. There was much debate over the two possible sources of the tsunami until high resolution bathymetry and multi-channel seismic studies performed by the US Geological Survey (USGS) during the first decade of the 21st century (Brink *et al.* 2004; Chaytor and ten Brink 2007, 2010) showed evidence of a submarine landslide. López-Venegas *et al.* (2008) used the identified geometry of the landslide, excavation area, and seismic reflection profiles to suggest the landslide as the most probable mechanism of generation of the tsunami, and ran simulations using the identified data to compare arrival times,

[1] Puerto Rico Seismic Network, Department of Geology, University of Puerto Rico, Mayagüez Campus, Mayagüez, PR, USA. E-mail: alberto.lopez3@upr.edu
[2] Texas A&M University at Galveston, Galveston, TX, USA. E-mail: horrillj@tamug.edu
[3] Department of Marine Sciences, University of Puerto Rico, Mayagüez Campus, Mayagüez, PR, USA.

Published online: 29 November 2014

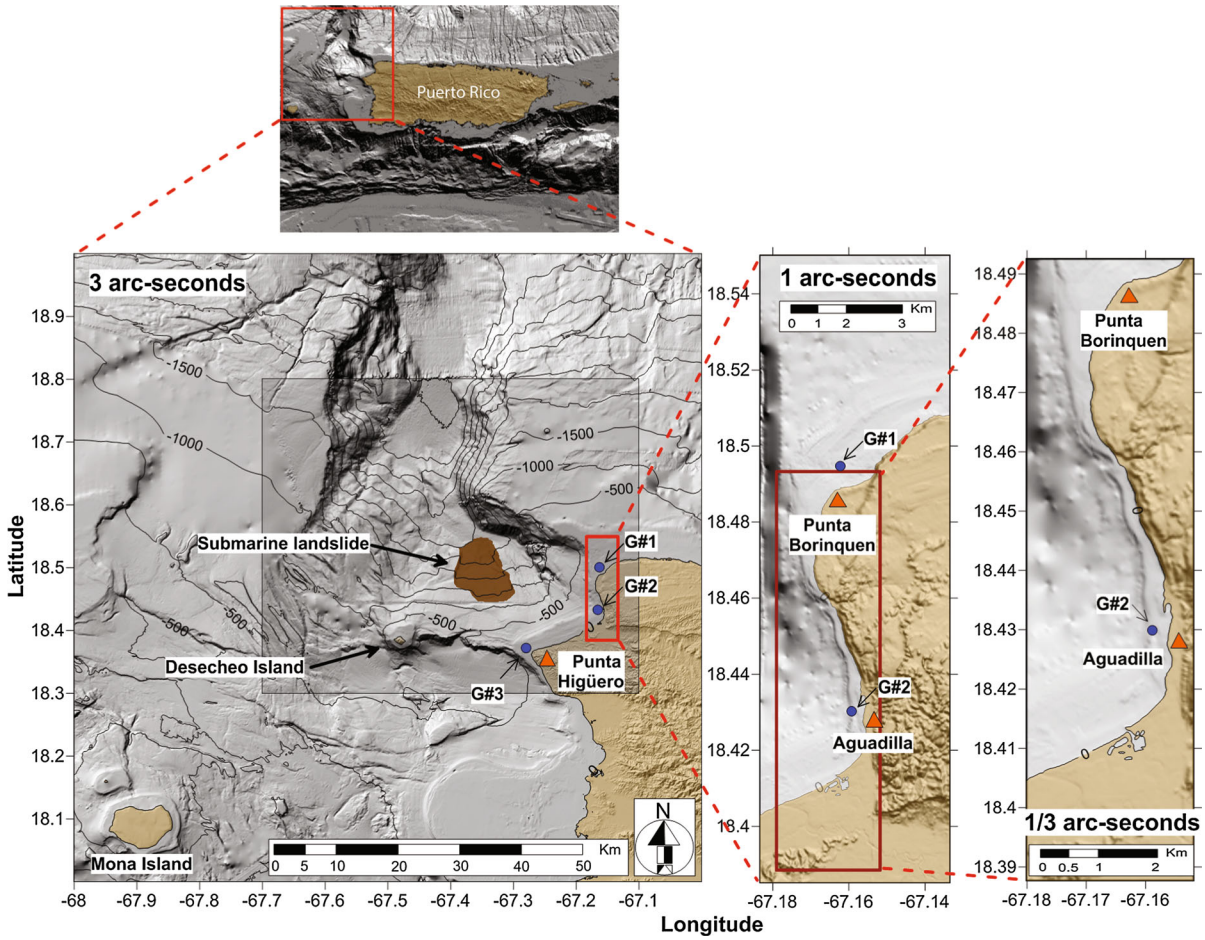

Figure 1
Bathymetry near Puerto Rico's northwest corner (Mona Passage) and nested domains (3, 1, and 1/3 arc-seconds of resolution) used by the 2D non-hydrostatic numerical model NEOWAVE for calculation of the tsunami wave propagation and runup. The generation domain (*gray shadow area* on the 3 arc-seconds domain) is used by the 3D numerical model TSUNAMI3D for calculation of the initial tsunami waves generated by the submarine landslide

polarity of the leading wave, and wave amplitudes close to the shore where runup values were measured by the post-tsunami survey of Reid and Taber (1919). In addition to the good agreement provided by the modeling, López-Venegas *et al.* (2008) favored the landslide over the dislocation model because historical evidence indicated two telegraph cables failed in the landslide generation area (Reid and Taber 1919) and no clear evidence of recent faulting or sea floor rupture was evident in either the seismic profiles or multi-beam bathymetry, respectively. Attempts to determine whether a submarine slide was the major source of the tsunami waves has been widely documented in the literature. For example analysis by Hornbach *et al.* (2008) suggested that a submarine slide was a plausible alternative explanation for generation of the 1918 tsunami.

Recent assessments of tsunami hazards along the Puerto Rico coastal regions conducted by the USGS have identified several large tsunamigenic submarine landslide scarps (Brink *et al.* 1999, 2004). The study has identified the presence of large scarps carved out on the northern margin of the Puerto Rico-Virgin Islands carbonate platform. The scarps show evidence that the northern slope of Puerto Rico has undergone massive submarine slope failures. As a consequence, massive underwater landslides in the vicinity of the Puerto Rico Trench are regarded as a

potential hazard (see also Dunbar and Weaver 2008) and the effects of such an event on the coastal region require further analysis with state-of-the-art numerical modeling tools. Thus, the purpose of this study was to re-assess the 1918 Mona tsunami by using a 3D–2D coupled numerical model which has its origin in two existing tsunami numerical models: the tsunami solution using the Navier–Stokes algorithm with multiple interfaces (TSUNAMI3D) (Horrillo 2006; Horrillo *et al.* 2013) and Non-hydrostatic Evolution of Ocean WAVE (NEOWAVE) (Yamazaki *et al.* 2009).

In the area in which the landslide was generated, the initial tsunami source is determined by use of the 3D Navier–Stokes (NS) model, TSUNAMI3D, developed by the University of Alaska Fairbanks (UAF) and the Texas A&M University at Galveston (TAMUG). The tsunami wave propagation and the detailed inundation is carried out by the 2D non-linear, non-hydrostatic/hydrostatic model NEOWAVE, developed by the UAF and the University of Hawaii (UH). Detailed energy analysis enabled us to determine the full development of the tsunami source and the appropriate time of coupling between the 3D and 2D models.

2. *Tsunami Source Description*

Strong evidence of a submarine landslide was present in USGS multibeam bathymetry data from the Mona Passage (Brink *et al.* 2007; Chaytor and ten Brink 2004) along the northern slope of the Desecheo Ridge, a shallow east-west trending ridge connecting the island of Desecheo with the western tip of Puerto Rico, in the Punta Higüero region, in the municipality of Rincón (G#3 in Fig. 1). The Desecheo Ridge is an important geologic feature in the Mona Passage because it separates the deepest portions of the Mona Rift leading to the Puerto Rico Trench to the north and the shallow Mayagüez Basin to the south (Chaytor and ten Brink 2010).

The shallowest portion of the landslide head scarp is located at latitude 18.44°N and longitude 67.49°W along the 1,320 m depth contour. Escarpments notable at both the left and right sides of the slide enable a detailed morphology of the landslide to be determined and an area of 76 km^2 to be computed (López-Venegas *et al.* 2008). Seismic reflection profiles covering the landslide region show the vertical extent of the excavation and portions of the depositional toe of the landslide. Most of the removed material from the landslide may be found dispersed throughout the Mona Rift and further north to the Puerto Rico Trench because the natural downslope in this region reaches deeper than 5,000 m. As a result, the landslide material is dispersed throughout the Mona Canal down to the Puerto Rico Trench, making it difficult to trace the depositional profile of the event. A more comprehensive description of the submarine landslide and the methodology used to obtain estimates of the volume of material removed are available elsewhere (López-Venegas *et al.* 2008).

López-Venegas *et al.* (2008) concluded that the geometry and orientation of the landslide favor an initial leading depression wave arriving at the western coast of Puerto Rico. Moreover, the combination of the distance of the slide from the shore and the bathymetry of the region leads to estimates of wave arrivals that are in agreement with the time between the onset of the earthquake and the arrival of the first observed wave, according to anecdotal evidence collected by Reid and Taber (1919). These factors are presented as crucial evidence in support of the landslide as the strongest candidate for generation of the tsunami. The north slope of the Desecheo Ridge is characterized by a northward, gently dipping carbonate platform featuring numerous faults and cracks. Violent ground shaking as a result of the earthquake must have dislodged sediment material along this gently dipping slope, resulting in generation of the tsunami.

In addition to presenting marine geophysical evidence to justify the landslide as the cause of the tsunami, López-Venegas *et al.* (2008) also performed tsunami simulations to estimate the landslide velocity and the bottom friction coefficient. The tsunami was simulated with COULWAVE (Lynett and Liu 2002) by using a crude rectangular rotational landslide with dimensions obtained from the bathymetry. Although simulations enabled determination of a landslide duration of 325 s and a best-fit bottom friction coefficient ranging from 0.01 to 0.04, the grids used (1,000 and 400 m) were too coarse to produce

detailed water amplitudes. Finally, limitations of the computational capabilities and the software at the time prevented inundation and runup computations, an objective this study seeks to accomplish by modeling a more realistic landslide flow with higher-resolution bathymetry.

3. Description of the Models

For development of inundation maps of landslide-generated tsunamis, a common approach is to combine a 3D Navier–Stokes (NS) model for the landslide-induced waves with a 2D depth integrated non-hydrostatic or Boussinesq model for the wave propagation and runup (coupled model). The 3D NS model is used to determine the wave kinematics and the free surface configuration caused by the landslide (the initial tsunami wave source); these are then input as the initial conditions (hot start) to the more numerically efficient 2D non-hydrostatic model for calculation of the wave propagation and detailed runup.

The 3D NS numerical model, TSUNAMI3D, is based on the computational fluid dynamic (CFD) model originally developed in Los Alamos National Laboratory (LANL) during the 1970s, and follows early work by Hirt and Nichols (1981). It solves transient fluid flow with free surface boundaries based on the concept of the fractional volume of fluid (VOF) method using an Eulerian mesh of rectangular cells of variable size. The fluid equations solved are the finite difference approximation of the full NS equation and the incompressibility condition equation which results from the continuity equation when the density is constant. The basic mode of operation is for a single fluid phase having multiple free surfaces. However, TSUNAMI3D also can be used for calculations involving two fluid phases separated by a sharp or diffusive interface, for instance, water and landslide material. In either case, both fluids are considered incompressible and treated as Newtonian. Internal obstacles, e.g., topography, wall, etc., are defined by blocking out, fully or partially, any desired combination of cells in the domain. It is well known that full 3D NS numerical models are highly computationally intensive and require substantial computer resources. Therefore, TSUNAMI3D has been simplified to overcome as much as possible the computational burden of 3D NS tsunami simulations. The simplification is derived from the large aspect ratio (horizontal and vertical scale) of the tsunami wave and the selected computational cell size required to construct an efficient 3D grid. The large aspect ratio of the tsunami wave also requires a large grid aspect ratio to reduce runtime and memory usage. However, the grid aspect ratio should be smaller than the aspect ratio of the tsunami wave to simplify the fluid surface reconstruction. The standard VOF algorithm, the donor–acceptor technique of Hirt and Nichols (1981), has been simplified to take into account this large cell aspect ratio. The pressure term is split into two components, hydrostatic and non-hydrostatic. Although TSUNAMI3D has the capability of variable grids (1D telescoping), it does not include the nesting capability (2D telescoping) needed for detailed inundation solutions on coastal regions. The interested reader is referred to Horrillo (2006) and Horrillo *et al.* (2013) for more detailed information about the 3D NS model.

The 2D depth-integrated and non-hydrostatic model NEOWAVE is built on the non-linear shallow-water equation with a non-hydrostatic pressure term to describe weakly dispersive waves. This approach is equivalent to existing models based on the classical Boussinesq equation. The model features a momentum conserved advection scheme that enables modeling of breaking waves without the aid of analytical solutions for bore approximation or empirical equations for energy dissipation. An upwind scheme extrapolates the free-surface elevation instead of the flow depth to provide the flux in the momentum and continuity equations. This scheme apparently improves the model stability which is essential for computation of energetic breaking waves and complex runups. The pressure term is split into hydrostatic and non-hydrostatic components, and the vertical velocity is introduced in response to the non-hydrostatic pressure through the three dimensional continuity equation. The interested reader is referred to Yamazaki *et al.* (2009) to obtain more detailed information about the 2D depth-integrated/non-hydrostatic model.

Both models, TSUNAMI3D and NEOWAVE, have led to very good agreement with the standards

provided by the National Tsunami Hazard Mitigation Program (NTHMP) for tsunami model validation and verification, report OAR-PMEL-135 (Synolakis *et al.* 2007). Results from validation and verification of these models can be also found in the NTHMP's Workshop Proceedings (NTHMP 2012).

3.1. 3D Navier–Stokes Model's Governing Equations

A schematic diagram of the domain and variables used in TSUNAMI3D is given in Fig. 2.

The governing equations used to describe the flow of two incompressible Newtonian fluids (e.g., water and landslide) are the incompressibility condition of the continuity equation:

$$\frac{\partial u_i}{\partial x_i} = 0, \quad i = 1,2,3 \tag{1}$$

and the nonconservative equation of momentum given by:

$$\frac{\partial u_i}{\partial t} + u_j \frac{\partial u_i}{\partial x_j} = -\frac{1}{\rho_{1,2}}\left(\frac{\partial p}{\partial x_i} + \frac{\partial q}{\partial x_i}\right) + \frac{\partial}{\partial x_j}\left[\frac{\mu_{1,2}}{\rho_{1,2}}\left(\frac{\partial u_i}{\partial x_j} + \frac{\partial u_j}{\partial x_i}\right)\right] + g_i, \quad i,j = 1,2,3 \tag{2}$$

where $u = [u(x,y,z,t),\ v(x,y,z,t),\ w(x,y,z,t)]$ are the velocity components along the coordinate axes $x = [x,y,z]$ at time t. Here, the given subscripts $1,2$ indicate physical variables corresponding to the water and landslide phases, i.e., $\rho_1(x,y,t)$ and $\rho_2(x,y,t)$ are the density of the water and landslide material, respectively. The water and landslide phases are considered as Newtonian fluids, therefore, the kinematic viscosity μ_1/ρ_1 and μ_2/ρ_2 can be adjusted for internal friction. Here μ_1 and μ_2 are the molecular viscosity of the water and landslide material respectively, thus, the landslide friction term in Eq. 2 factored by μ_2/ρ_2 can be adjusted according to a constitutive model for landslide rheology, e.g., the Bingham model, which is not implemented in this study. The acceleration due to gravity is represented by $\mathbf{g} = [\mathbf{0}, \mathbf{0}, -\mathbf{g}]$. The total pressure in each phase, $p_{\text{tot}} = p + q$, is divided into the hydrostatic pressure p and the dynamic or non-hydrostatic pressure q.

In the water domain the hydrostatic pressure is given by:

$$p = \rho_1 g(\eta_1 - z) \tag{3}$$

such that $\partial p/\partial z = -\rho_1 g$. Here, z is the elevation measured from the vertical datum to the cell center and η_1 is the water free surface elevation, also measured from the vertical datum.

For the landslide phase, the total pressure $p_{\text{tot}} = p + q$, is determined by the hydrostatic pressure as:

$$p = g[\rho_1(\eta_1 - \eta_2) + \rho_2(\eta_2 - z)] \tag{4}$$

and the dynamic pressure q. Here η_2 is the landslide free surface elevation measured from the vertical datum. The landslide material is also considered as a Newtonian fluid, with kinematic viscosity, μ_2/ρ_2 for internal friction.

Both water and landslide surface elevations, η_1 and η_2, are traced using the simplified VOF method based on the scalar function F and the donor-acceptor algorithm of Hirt and Nichols (1981). The method is

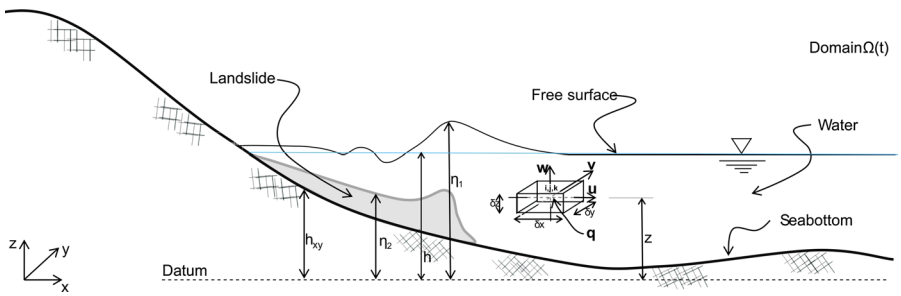

Figure 2
Sketch of model domain and variables for 3D NS model TSUNAMI3D

based on the so-called fraction function F, in which F is defined as the fraction of fluid in the control volume cell (namely, volume of a computational grid cell). F is a discontinuous function, its value varies from 0 to 1 depending of the fluid interface location. Basically, when the cell is empty, the cell has no fluid inside and the value of F is zero; in contrast, when the cell is full, $F = 1$; therefore, when the fluid's interface is within the cell, $0 < F < 1$. Details of the simplified VOF method can be also found in Horrillo *et al.* (2013).

For discretization of the computational domain, the model uses an Eulerian variable mesh of rectangular cells with large aspect ratio. The governing equations are solved by using the standard explicit finite difference scheme starting with field variables such as **u**, q and $\eta_{1,2}$ known at time $t = 0$. The governing equations are solved by discretizing the field variables spatially and temporally in the domain to obtain new field variables at any required time. All variables are treated explicitly with the exception of the non-hydrostatic pressure field, q, which is implicitly determined (Casulli and Stelling 198). Nonlinear terms are approximated by using an up-wind down-wind approach up to the third order (Horrillo *et al.* 2013). The hydrodynamic pressure field q is calculated by use of Poisson's equation, by using the incomplete Choleski conjugated gradient method to solve the resulting linear system of equations.

The friction term in the momentum equation can be adjusted to mimic the internal friction within the fluid body, i.e., the viscosity coefficient. This coefficient has been chosen to give the best possible agreement with the reference data.

3.2. 2D Non-Hydrostatic Model's Governing Equations

The governing equations for the depth-integrated, non-hydrostatic NEOWAVE model (Yamazaki *et al.* 2009), are derived from the incompressible Navier–Stokes equation and the incompressibility condition of the continuity equation in a spherical coordinates system in which λ is the longitude, ϕ is the latitude, and z denotes the normal distance from the still water level (SWL). The resulting momentum equations along λ, ϕ, z directions are:

$$\frac{\partial U}{\partial t}+\frac{U}{R\cos\phi}\frac{\partial U}{\partial \lambda}+\frac{V}{R}\frac{\partial U}{\partial \phi}-\left(2\Omega+\frac{U}{R\cos\phi}\right)V\sin\phi = -\frac{g}{R\cos\phi}\frac{\partial \zeta}{\partial \lambda}-\frac{1}{2}\frac{1}{R\cos\phi}\frac{\partial Q}{\partial \lambda}-\frac{1}{2}\frac{Q}{DR\cos\phi} \times\frac{\partial(\zeta-h_b+\eta_{co})}{\partial \lambda}-n^2\frac{g}{D^{1/3}}\frac{U\sqrt{U^2+V^2}}{D} \quad (5)$$

$$\frac{\partial V}{\partial t}+\frac{U}{R\cos\phi}\frac{\partial V}{\partial \lambda}+\frac{V}{R}\frac{\partial V}{\partial \phi}+\left(2\Omega+\frac{U}{R\cos\phi}\right)U\sin\phi = -\frac{g}{R}\frac{\partial \zeta}{\partial \phi}-\frac{1}{2}\frac{1}{R}\frac{\partial Q}{\partial \phi}-\frac{1}{2}\frac{Q}{DR}\frac{\partial(\zeta-h_b+\eta_{co})}{\partial \phi} -n^2\frac{g}{D^{1/3}}\frac{V\sqrt{U^2+V^2}}{D} \quad (6)$$

$$\frac{\partial W}{\partial t}=\frac{Q}{D} \quad (7)$$

and the continuity equation reads:

$$\frac{\partial(\zeta-\eta_{co})}{\partial t}+\frac{1}{R\cos\phi}\frac{\partial(UD)}{\partial \lambda}+\frac{1}{R\cos\phi}\frac{\partial(VD\cos\phi)}{\partial \phi}=0 \quad (8)$$

where U, V and W are depth-averaged velocity components in the λ, ϕ and z directions respectively. The variable t is the time, ζ is the free surface elevation from the SWL, R is the Earth's radius, Ω is the Earth's angular velocity, ρ is the water density, Q is the non-hydrostatic pressure, g is the gravitational acceleration and n is the Manning's coefficient for the sea-bottom friction. The vertical velocity W is assumed to have a linear distribution along the water column, therefore the vertical velocity component W is simply the average value of the vertical velocity at the free surface and the sea floor. The total depth is defined as $D = \zeta + (h_b - \eta_{co})$, where h_b is the water depth (from SWL to sea floor) and η_{co} is the sea floor co-seismic deformation (η_{co} is not considered in this study). A detailed discussion of NEOWAVE numerical scheme, solution and capability is found in Yamazaki *et al.* (2009).

4. 3D–2D Coupling Process

One critical step in the process of coupling the two models is to determine the right moment to transfer the 3D model's wave and water kinematic (u, v and w) and free surface (η_1) field to the 2D non-hydrostatic

model. The right time for transfer is determined by the 3D domain size, and the total energy of the water induced by the submarine landslide. The 3D domain must be large enough to fully develop the generated waves without leaving the domain boundaries, and the wave energy should reach a maximum which indicates that the generated waves are fully or mostly developed. If the domain size-energy considerations have been fulfilled, then the 3D field information or variables (u, v, w and η_1) are converted into two dimensions by simple column-wise depth averaging and input as the initial condition (hot start) to the 2D non-hydrostatic numerical model.

4.1. Energy Equations

The generated waves are determined to have been fully developed when the total (potential plus kinetic) wave energy reaches a maximum. Energy in the system (3D domain) is determined at each phase (water and landslide) from the equations of classical mechanics by integrating each control volume or computational cell energy over the entire domain. The potential energy of the deformed water surface is measured in terms of $\eta_1 - h$, the free surface elevation from the SWL (Fig. 2). The wave's potential energy per unit horizontal area is given by:

$$E_{P_{\text{Water}}} = \frac{1}{2}\rho_1 g(\eta_1 - h)^2. \tag{9}$$

The water or wave's kinetic energy is a function of the square of the velocity:

$$E_{K_{\text{Water}}} = \frac{1}{2}m_1(u^2 + v^2 + w^2) \tag{10}$$

where m_1 is the mass of the water fraction (F) in the control volume.

The energy of the landslide material can be calculated in a similar manner. The potential energy of the landslide material is measured in terms of the submerged sediment density $\rho_2 - \rho_1$ and the distance of the landslide surface η_2 from the vertical datum. The landslide potential energy per unit horizontal area is then given by:

$$E_{P_{\text{Slide}}} = \frac{1}{2}(\rho_2 - \rho_1)g(\eta_2 - h_{xy})(h_{xy} + \eta_2) \tag{11}$$

where h_{xy} is the height of the sea floor from the vertical datum (Fig. 2). The landslide kinetic energy equation is again similar to that of the water:

$$E_{K_{\text{Slide}}} = \frac{1}{2}m_2(u^2 + v^2 + w^2) \tag{12}$$

with m_2 the mass of the fraction (F) of the landslide material in the control volume. Assuming a still water condition at $t = 0$, all energies are zero except for the potential energy of the landslide ($E_{P_{\text{Slide}}}(0)$), which has a value based on the landslide's location relative to the reference vertical datum. At any time t, the change in landslide potential energy $E_{P_{\text{Slide}}}(0) - E_{P_{\text{Slide}}}(t)$ gives the amount of energy released into the system at that time.

Similar energy analysis was performed by Abadie *et al.* (2012) using a 2D numerical model for a landslide tsunami and by Sue *et al.* (2006) using a block slide experimental arrangement. Abadie *et al.* (2012) calculated potential and kinetic energy of the water/wave ahead of the landslide by integrating the energies from the tip of the landslide to the boundary of the computational domain. Sue *et al.* (2006) used data measurements to calculate potential and kinetic energy of the block landslide and the potential energy of the resulting wave, thereby relating the energy of the landslide to the energy transferred to the wave. Here, we are able to perform a more comprehensive 3D energy analysis as the potential and kinetic energy of the wave and landslide can easily be calculated separately in time by integrating the respective energies from each computational cell, depending on the cell's fractional amount of water and/or landslide material. This results in a more complete view of the complex energy behavior in landslide motion, tsunamigenesis, and physical/numerical losses.

5. Results: 3D Landslide-Tsunami Simulation

The model TSUNAMI3D was used to perform the full-scale 3D numerical simulation to calculate the initial tsunami wave on the basis of our assumption that the earthquake initiated an underwater landslide. The resulting mass wasting of the Mona tsunami underwater landslide is approximately 155 m thick

(on average), ~10.5 km long, ~7.7 km wide and slides (initially) over a slope of ~10 %. The wasting volume of ~12.5 km^3 used in this numerical simulation is larger than that of 10.0 km^3 reported by López-Venegas *et al.* (2008) and ten Brink *et al.* (2006). The discrepancy is attributed to the different slide dimension obtained by following more precisely the scarp borders and, probably, to the different method used for calculation of the volume. The landslide volume reported herein was calculated by projecting tangentially the existing immediate isobath located at the undisturbed edges of the scarp to create smooth surfaces between the projected isobath, gridding these smooth surfaces, and subtracting these surfaces from the gridded bathymetry of the scarp. In contrast, the landslide volume reported by López-Venegas *et al.* (2008) and ten Brink *et al.* (2006) was calculated by interpolating smooth surfaces through polygons that define the edges of the slide.

Figure 1 shows the bathymetry of the Puerto Rico's northwest corner that surrounds the Mona scarp. The shadowed region on Fig. 1 indicates the 3D domain used by the TSUNAMI3D model. The 3D domain dimension box is 0.6 arc-degree (east-west) × 0.5 arc-degree (south-north) and 5.10 km high. The south-north horizontal dimension of the domain is approximately 55.6 km long, and at latitude of ~18.55N arc-degrees the east-west horizontal dimension is approximately 63.26 km long. The domain grid resolution is 720 × 600 × 337 cells in the x, y and z direction, respectively, for a total of 145.6 million cells. Thus, the model's horizontal spatial steps are 87.86 × 92.67 m (x, y) and the vertical spatial step is variable, and ranges from 1 to 8 m. The finer vertical resolution was confined in the water-free surface and water–landslide interface regions, in contrast with the coarser vertical resolution which was confined to the deeper-water regions. The time step size is variable with a minimum value of 0.05 s. The seawater and landslide densities have assigned values of 1,025 and 2,000 kg/m^3, respectively. A Newtonian fluid approach has been assumed for the water-landslide system; the viscosity coefficients (kinematic viscosity) μ_1/ρ_1 and μ_2/ρ_2 have been set to 1×10^{-6} m^2/s as a conservative assumption to obtain greater landslide downslope acceleration, tsunami wave amplitude, and runup. The free slip condition is applied in all fluid cells neighboring a sea bottom cell, i.e, $\partial \mathbf{u}/\partial z = 0$. In an early state of a full-scale landslide downslope movement, a Newtonian fluid assumption for the landslide material is reasonably valid if one seeks a conservative initial tsunami wave. It is also true that a Newtonian fluid will not come to rest completely. However, the initial tsunami wave characteristic is mainly controlled by the early landslide kinematics and slide characteristics (initial slide acceleration, size, slope, sediment properties, etc.) and not by the subsequent slide evolution in deeper water. As the landslide reaches deeper water, the effects of the landslide kinematics only cause minor changes to the main tsunami characteristics (Haugen *et al.* 2005; Grilli and Watts 2005; Watts *et al.* 2005). It is also observed that massive landslides have longer runout distances. Basal-friction and shear-rate seem to reduce as the landslide thickness and volume increases. The larger the slide volume, the greater the thickness and the smaller the shear rate (Campbell *et al.* 1995). Therefore, assumption of no basal friction in the initial state of wave generation, or even assuming an almost inviscid flow for the landslide-water system, are valid and conservative suppositions for a full-scale event. The geological range in deeper water of many large fan systems originating from ancient submarine landslides supports this simplified assumption of a Newtonian fluid for the landslide material.

Using a cluster with 32 CPUs assigned, computer time required to simulate 10 min of the Mona Passage underwater landslide and tsunami was ~48 h.

The 3D simulation results of the landslide-induced tsunami waves are shown in Fig. 3. The left panels of Fig. 3 show snapshots of the evolution of the underwater landslide at 0.5, 1.5 and 3 min; the respective evolution of the free surface is shown in the right panels. As is apparent from Fig. 3 (use the color bar as a reference), a wave ~48 m high (crest to trough) is recorded 3 min after slide initiation. The outgoing positive wave with an amplitude of ~18 m is followed by a backgoing negative wave or initial surface depression of ~30 m caused by the fast downslope motion of the underwater landslide. Notice that a rebounding wave is emerging from the surface depression between the outgoing and the negative backgoing wave (Fig. 3b, c). The

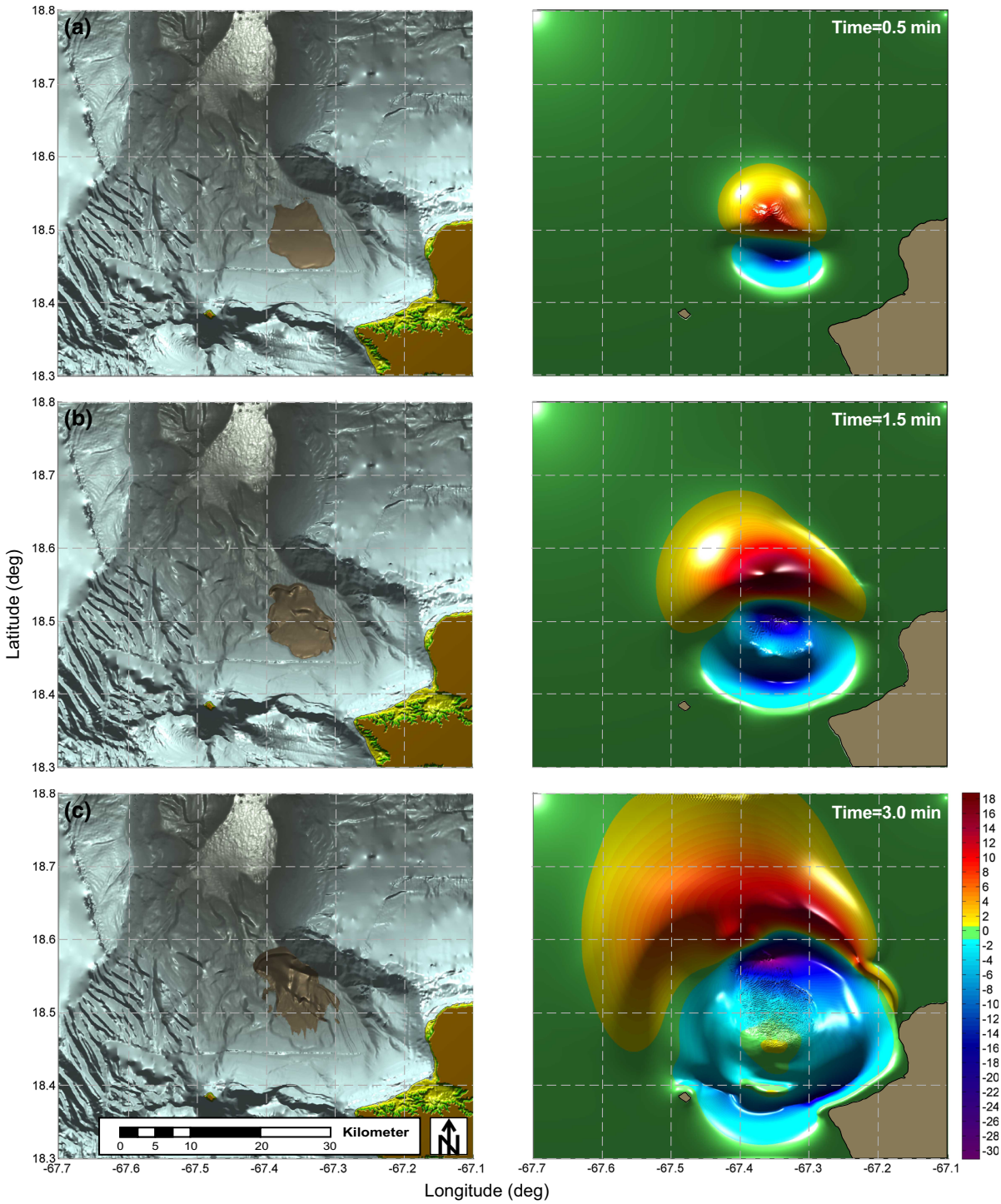

Figure 3
TSUNAMI3D results: submarine landslide evolution (*left column*) and tsunami wave evolution (*right column*) after 0.5 min (*top row*), 1.5 min (*mid row*) and 3 min (*bottom row*). *Color bar* in meters

rebounding wave does not evolve as a massive wave in the same way as the outgoing wave, but as a short and highly dispersive wave.

5.1. Landslide and Tsunami Energy

The energy produced by the landslide and resulting tsunami wave is presented in Fig. 4. Figure 4a shows the change of potential energy and the kinetic energy of the landslide. The change of the landslide potential energy is presented as the difference between the initial potential energy and the potential energy at time t, $E_P(0) - E_P(t)$. This difference accounts for produced energy that is released at time t into the system after the landslide motion begins ($t = 0$). The landslide kinetic energy initially increases and then begins to level off after $\sim$160 s. As mentioned above, the assumption of a Newtonian fluid means the landslide material will not come to a complete rest, therefore the energy produced continues to increase, but the landslide stops accelerating after less than 3 min. As found by Sue *et al.* (2006), the initial change of potential energy of the landslide is converted mostly into landslide kinetic energy as the landslide begins moving, i.e., $t < 40$ s. This kinetic energy is then transferred into the kinetic energy of the water as the moving landslide sets the water around it into motion. The water movement deforms the free surface, converting some of the water kinetic energy into potential wave energy. For example, at an early state (<20 s) after the onset of the landslide, the potential energy given off by the landslide is mostly converted to landslide kinetic energy. Also during this time a small fraction of the landslide potential energy inside the generation area starts to be converted to water kinetic energy and wave potential energy (Fig. 4b) with values one and two orders of magnitude smaller.

We partition the water energy on the basis of the location of the landslide to account for the energy that propagates away from the wave generation area separately from the energy inside the generation area (Abadie *et al.* 2012). The outgoing and backgoing propagating waves, which are those that propagate outside the generation area, are of principal interest for tsunami inundation and hazard assessment. Also, we determine the development of the tsunami wave in terms of the energy released in the system on the basis of the energy outside the generation area and thus the appropriate time to transfer the wave information from the 3D model (TSUNAMI3D) to the 2D model (NEOWAVE). The generation area is defined in time by flagging computational cells horizontally surrounding the landslide; here, we mask four cells on any side of a cell which contains landslide material at any point in time, resulting in a 9×9 horizontal grid surrounding any landslide cell. Inside the generation area, the kinetic water energy is summed on water cells column-wise from the surface of the landslide to the free water surface, and outside the generation area this kinetic energy is summed on water cells column-wise from the sea floor to the free water surface.

Figure 4b shows the potential and kinetic energy of the water inside the generation area; likewise, Fig. 4c shows the water energy outside the generation area. Clearly, we see that the water kinetic energy is substantially affected by the landslide motion, because the kinetic energy of the water in the generation area continues to increase substantially with the continued landslide motion and is approximately one order of magnitude larger than the kinetic energy outside the generation area (compare the dashed lines in Fig. 4b, c). However, inside the generation area the potential water energy is almost two orders of magnitude less than the kinetic energy and reaches a maximum early (after $\sim$62 s; apparent from the magnification in Fig. 4b) as the initial wave begins to leave the generation region. Outside the generation area, Fig. 4c, the wave potential energy is approximately twice as large as that inside the generation area, because of the large amplitude of the initial tsunami waves and the subcritical regime (Froude number $F_r = V_s/\sqrt{gD} < 1$, where V_s is the average landslide velocity, D the total water depth, and g the acceleration due to gravity) for this specific underwater landslide. The potential and kinetic energy of the water outside the generation region level off or reach a maximum in approximately 180 s (3 min). Effectively, once the initial large wave propagates from the generation region, its energy stabilizes. Whereas Abadie *et al.* (2012) found equipartition of wave energy away from the landslide as very nearly half potential and half kinetic, the

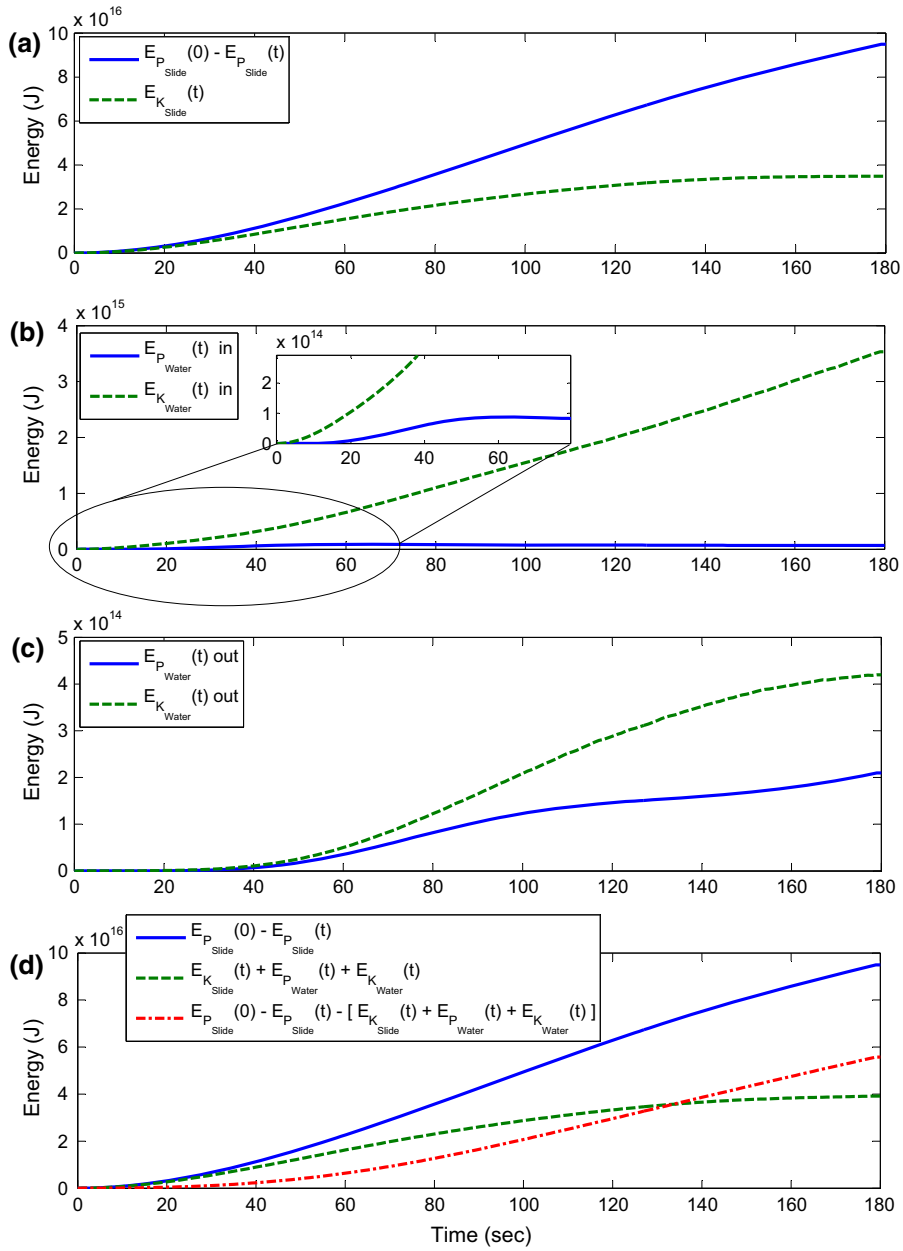

Figure 4

Potential-released and kinetic energy of the landslide and resulting wave inside and outside the wave generation area. **a** Potential energy released by the landslide (*solid line*) and kinetic energy of the landslide (*dashed line*). **b** Potential (*solid*) and kinetic (*dashed*) energy of the water inside the generation area. **c** Potential (*solid*) and kinetic (*dashed*) energy of the water outside the generation area. **d** Comparison between the potential energy released by the landslide and the total energy transferred to the system (landslide kinetic + water kinetic + water potential)

kinetic energy determined here is approximately twice as large as the potential energy; this difference is most likely because equipartition of energy may not be valid immediately during the process of generation of the wave (Fritz *et al.* 2004; Watts 2000). The large difference might be enhanced by inclusion of the third spatial dimension, in contrast with the 2D model in Abadie *et al.* (2012).

Equipartition of water energy outside the generation area is expected to occur later in the wave-propagation process.

As a result of these energy calculations, we conclude that most of the energy transfer from the landslide to the wave occurs in the first few minutes of wave generation, as also found by Abadie *et al.* (2012). Conversion of potential energy into water energy in this 3D deep-submerged landslide is between 3.5 and 4.5 %, similar to that for other studies of submerged landslide [Watts (2000), 3–7 % of the landslide kinetic energy; Sue *et al.* (2006], 1.1–5.9 % of the landslide potential energy). Although substantial wave-energy production continues within the generation region, the increasing depth of the landslide limits any further tsunamigenic potential after the initial wave is formed. Therefore, the tsunami wave is mostly developed by the time it reaches the boundary of the computational domain and 3 min is an appropriate time to transfer the wave information from TSUNAMI3D to NEOWAVE for the detailed inundation calculation.

The total energies are compared in Fig. 4d. The solid line shows the total energy input into the system by the landslide potential energy and the dashed-dotted line represents the energy loss. In a closed system, the potential energy released by the landslide would be converted completely into landslide kinetic energy plus total water/wave energy (dashed line). However, there is a substantial difference between these energies in our model result. This is a topic of continued study, but we believe this is largely because of numerical diffusion which is expected to be more substantial in a 3D numerical model. Nevertheless, we still are able to include small additional friction through the viscosity coefficient while keeping basal friction negligible, meaning that "physical friction" is kept to a minimum. In more realistic or complex models, for example, in a domain with complicated bathymetry as in this particular case, we are aware that numerical models undergo substantial numerical diffusion or energy dissipation in regions where waves shoal or runup. The numerical diffusion effect is well observed when waves travel over a sloping sea bottom (Kowalik 2008), because the nonlinear terms are usually reduced to an upstream/downstream numerical form. For example, in a 1D x direction scheme, the numerical diffusion associated with the first order of approximation (positive velocity) for the nonlinear term reads:

$$\frac{u_p h_x}{2}\frac{\partial^2 u}{\partial x^2} \tag{13}$$

where u_p is the resulting water or slide downstream particle velocity from the upstream/downstream numerical scheme, and h_x is the space step or the x direction grid resolution. This term (Eq. 13) is similar to the friction term in the momentum equation (Eq. 2) with viscosity coefficient (artificial-numerical viscosity $u_p h_x/2$) being a function of the space step h_x and the downstream particle velocity u_p. The artificial-numerical viscosity coefficient is large in shallow water regions where wave particle velocities are larger, enhanced further by the shoaling or slope gradient. In contrast, in deeper water with a uniform or smooth sea bottom bathymetry, particle wave velocities (i.e., u_p) are very small and the numerical diffusion caused by the nonlinear terms is also small. In these regions, numerical diffusion occurs in the short-wavelength range, being determined by how well short waves are resolved by the spatial step. Waves generated by submarine and subaerial landslides are very dispersive and are degraded quickly into short waves; therefore, the model's numerical scheme will quickly dissipate these short waves that are at or close to the unresolved scale ($2h_x$) (Kowalik 2008).

In addition, a depth-profile of the wave kinetic energy density in J m^{-3} within the wave-generation area is shown in Fig. 5. This seems to be an interesting analysis of the energy behavior within the water column and enables further understanding of the water dynamics associated with the landslide. The kinetic energy density of the wave is largely concentrated near the landslide, which reaches from a depth of approximately $-1{,}200$ to $-3{,}000$ m initially, and $-1{,}200$ to $-3{,}500$ m after 3 min. The depth interval of main energy concentration grows with time, so that the energy imposed by the landslide reaches higher into the water column, but it is mainly concentrated deeper than $-1{,}200$ m. There is a small amount of energy density at the surface associated with free surface motion, but it is minimal compared with the maximum at greater depth. At the beginning,

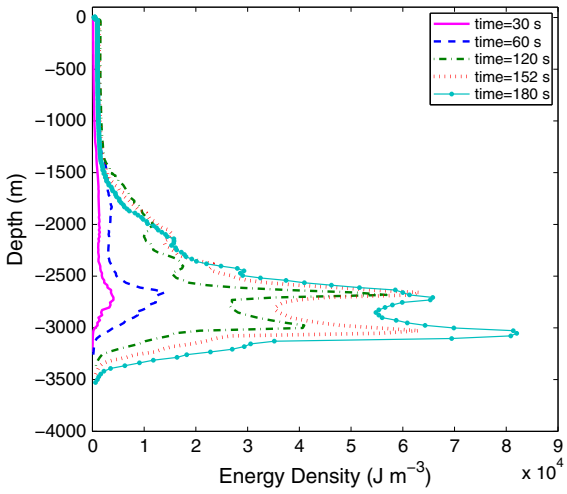

Figure 5
Depth profile of water kinetic energy density within the generation area at selected times during wave generation

the energy density maximum occurs just above the leading edge of the landslide. This maximum may also be amplified at later times (after ∼120 s) by rebounding of landslide material from the face of a cliff in the sea floor. A secondary maximum occurs over the middle part of the landslide at earlier times (before approx. 60 s), then becomes increasingly pronounced above a deepening portion of the leading edge. Interestingly, at 152 s, the energy densities above the shallower and deeper portions of the leading edge are nearly balanced, and thereafter the maximum energy density shifts to the deeper portion, with the energy near the shallower part becoming a secondary maximum as the leading edge smooths and flattens. At 3 min, when the wave information is transferred to the 2D model, a maximum energy density of 8.2×10^4 J m^{-3} is calculated at −3,052 m depth.

5.2. *Inundation and Run-up*

By using the numerical code NEOWAVE with the nested grids shown in Fig. 1, detailed tsunami runup was obtained in present-day Aguadilla, i.e., sea-level elevation (runup), water depth (inundation) and maximum momentum flux quantities. Figure 6 shows the tsunami inundation results in Aguadilla calculated on the innermost grid (1/3 arc-second resolution) of the nested grid domain. Figure 6a shows the maximum runup or sea-level elevation with reference to the mean high water (MHW) level. Figure 6b shows the inundation depth defined as $D = \zeta - h$; where ζ is the sea-level elevation and h is the land elevation with respect to the MHW level. It is important to mention that regions with inundation depth shallower than 1 ft (∼0.30 m) are not indicated in the figure. Numerical results show that the overall maximum water elevation in the populated area of present-day Aguadilla ranges from 3 to 9 m. Consequently, the maximum inundation depth ranges from 0.30–6.0 m.

Three nearshore numerical gauges have been located in the domain to record the profile in time of the tsunami waves as they approach Puerto Rico's western coastal region (Fig. 1). Table 1 shows the location of the numerical gauges; their results are depicted in Fig. 7.

According to Reid and Taber's survey, all locations in western Puerto Rico experienced a tsunami leading depression wave. In the Old Lighthouse (Punta Borinquen—G#1), the lighthouse keeper observed the sea receding shortly after he felt the main shock, whereas the Rincón lighthouse keeper at Punta Higüero (G#3) witnessed the sea returning ∼2 min after it receded shortly after the earthquake. Several important observations can be derived from the numerical simulation results. The initial wave to approach the shore was indeed a negative wave, and this negative wave reached the coastline facing Aguadilla approximately 5 min after initiation of the landslide (G#2 wave profile, middle panel of Fig. 7). This is consistent with the arrival time observations reported by Reid and Taber (1919) and the computations of Mercado and McCann (1998), who used a dislocative source, and López-Venegas *et al.* (2008), who used a submarine landslide source.

Our simulations yield a maximum wave amplitude of 2.2 m at 13 m depth offshore of the coast at Punta Borinquen (upper panel of Fig. 7), with on-shore runup of 4.8 to ∼5.4 m (color scale inside the upper red triangle indicating the location of the Old Lighthouse in Fig. 6a). The runup model result is slightly higher than the estimated 4.6 m on-shore runup value from the post-tsunami survey, but much

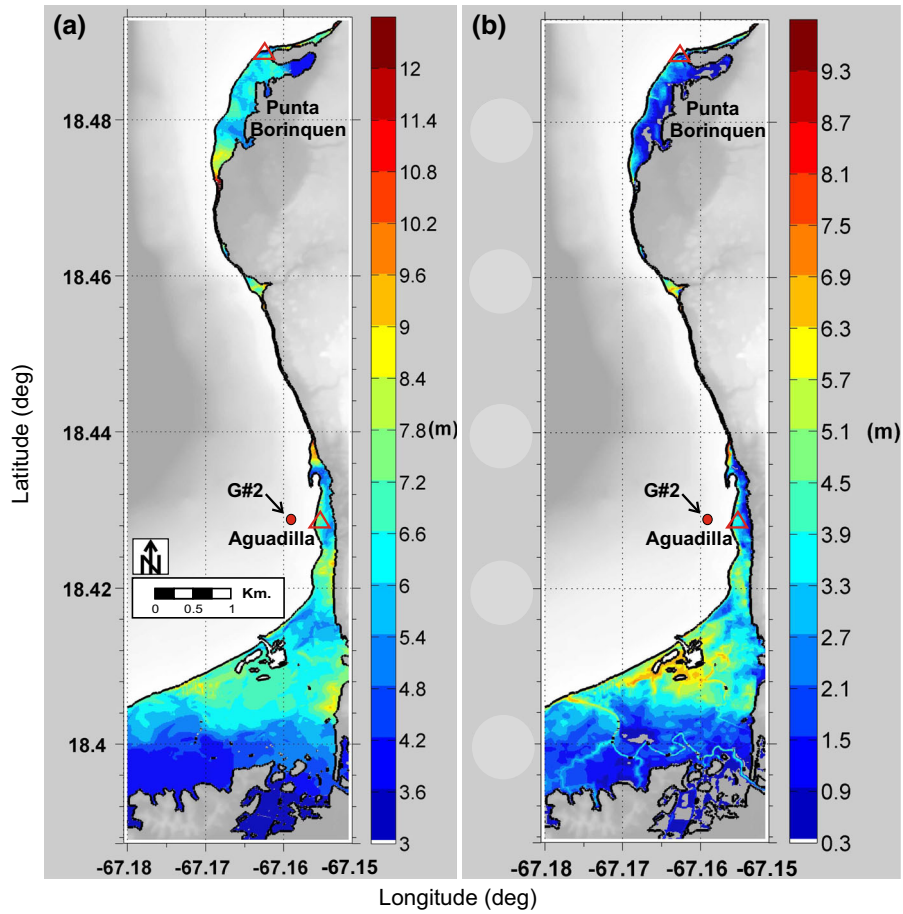

Figure 6
Numerical results for Aguadilla calculated on the innermost grid (1/3 arc-second resolution) of the nested domain. **a** Maximum runup or sea-level elevation. **b** Maximum inundation depth

Table 1

Numerical gauge location

Gauge number[a]	Station name	Longitude (°W)	Latitude (°N)	Water depth (m)
G#1	Old Lighthouse (Punta Borinquen)	67.162423	18.494596	13.0
G#2	Aguadilla	67.161112	18.429514	36.0
G#3	Rincón Lighthouse (Punta Higüero)	67.274675	18.364380	15.0

[a] See Fig. 1 for gauge location

lower than the 8.3 m obtained from the previous modeling study of López-Venegas *et al.* (2008). At the numerical gauge offshore of Aguadilla (G#2) (middle panel of Fig. 7), the model's maximum wave amplitude of the approaching wave is estimated at 4.2 m at a depth of 36 m, and the runup in the area of the old downtown (lower red triangle in Fig. 6a) ranges from 4.8 to 7.2 m. These values are in agreement with the >4.0 m values estimated by the survey and still substantially lower than the 12.8 m estimated by López-Venegas *et al.* (2008). The extent of flooding of Aguadilla predicted by the model (partial flooding of the town square West of San Carlos Borromeo Church, two blocks east of the beachfront) is accurate (Fig. 8). Witnesses reported that the tsunami penetrated up to the town square but not to the Church. Finally, for the third numerical gauge (G#3) at Punta Higüero, which is located at a depth of 15 m, wave maximum amplitude is estimated to be 7.1 m.

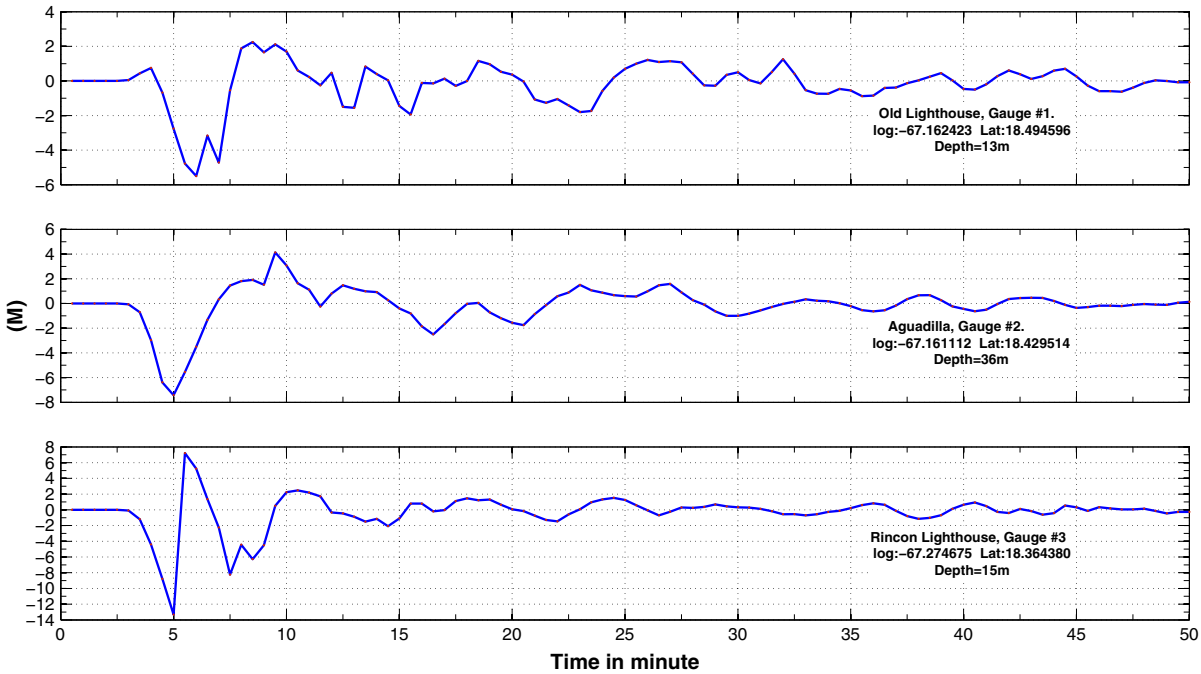

Figure 7
Numerical gauge results at three different locations indicated in Table 1 and previously surveyed by Reid and Taber (1919). *Top panel* (G#1), Old Lighthouse at Punta Borinquen; *middle panel* (G#2), Aguadilla; *bottom panel* (G#3), Rincón Lighthouse at Punta Higüero. The locations of the gauges are given in Fig. 1

Surprisingly, the positive wave came shortly after the negative wave, as was witnessed by the Rincón lighthouse keeper (lower panel in Fig. 7). Unfortunately, this location is outside the 1/3 arc-second grid, thus detailed runup was not computed. However, high on-shore runup values were not in agreement with either the survey of Reid and Taber (1919) (5.5 m) or the results of López-Venegas *et al.* (2008) (5.9 m). In this particular region, the topography features coastal cliffs and shallow water. Therefore, a nested grid with increasing resolution should be considered in future research to estimate precisely the runup and extent of inundation near the Rincón lighthouse at Punta Higüero.

Our results are in better agreement with the values obtained from the post-tsunami survey of Reid and Taber (1919) than those obtained from the previous numerical model of López-Venegas *et al.* (2008). Therefore, we conclude that simulations at both G#1 and G#2 fit the observations well whereas the simulation might slightly overestimate at G#3. These values are corroborated by the NEOWAVE inundation simulation in Fig. 6. The fact that slightly higher values are obtained is related to the internal friction of the landslide, which here is kept to a minimum to estimate potential damage for the present-day coast if a similar event were to happen today.

Although the main motion of the landslide was directed toward the north, some of the energy of the tsunami was refracted around Puerto Rico's northwest shelf, producing waves affecting Puerto Rico's north coastline. A separate study is in progress to quantify these effects, because these waves would be highly dispersive for a landslide source, thus enabling discrimination among the postulated sources.

5.3. *Momentum Flux*

The magnitude of tsunami momentum flux was also calculated, to determine the potential for inland damage from the flow forces. The magnitude of momentum flux could be useful for engineering design purposes, for re-assessment of existing structures, for

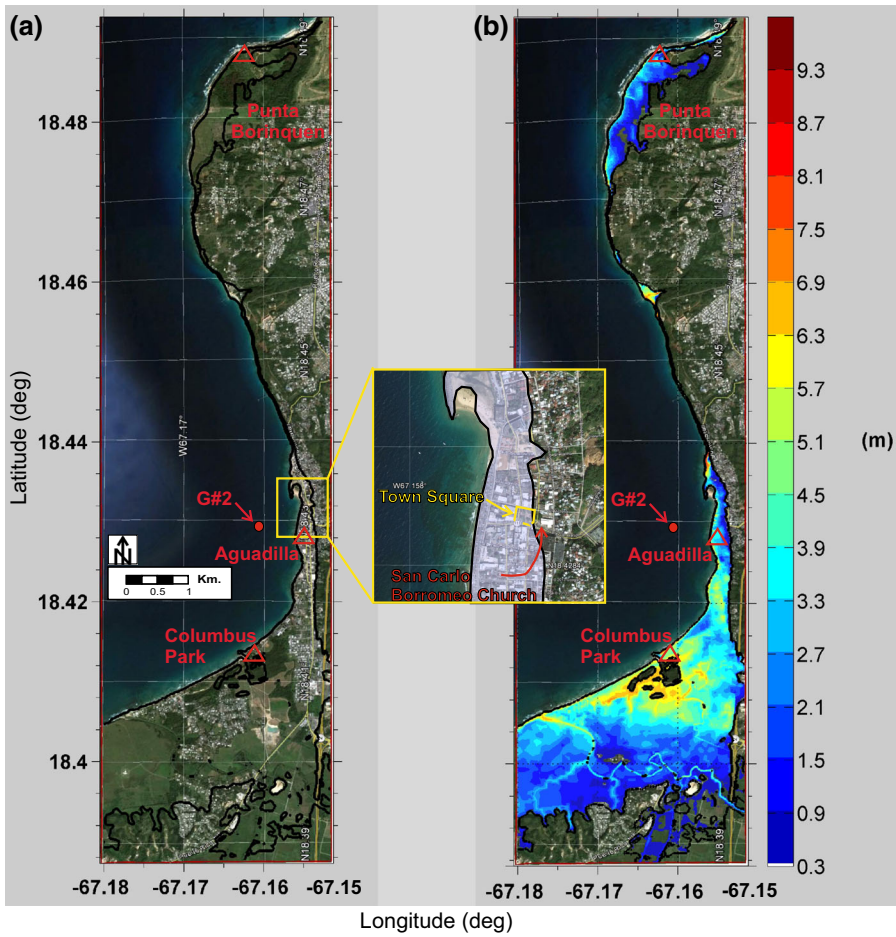

Figure 8
Extent of inundation by the Tsunami in present-day Aguadilla (northwest Puerto Rico) assuming the hypothetical case of the Mona tsunami of October 11, 1918. **a** Inundation limits map. **b** Inundation depth map, are placed side by side to facilitate visualization of the inundation level in relation to populated areas. The *plan view* is taken from Google Earth©

assisting coastal managers in assessing the relative vulnerability of some infrastructure, or in identifying the nature and location of major tsunami flows. Figure 9 shows the magnitude of the inundation depth and water flow velocity at maximum momentum flux. The inundation depth shown in Fig. 9a corresponds to the inundation depth at the time when the maximum momentum flux occurs. It is important to mention that this inundation depth is slightly different from the maximum inundation depth portrayed in Fig. 6b. In the same manner, the flow velocity, shown in Fig. 9b corresponds to the velocity when the maximum momentum flux occurs. These quantities are valuable for determination of flow forces on sensitive structures along the tsunami runup path.

Assuming steady flow, the inundation forces exerted on a surface-piercing structure can be evaluated by use of the hydrodynamic force equation:

$$F = \frac{1}{2}\rho C_{\mathrm{d}}(b \times h)u^2 \tag{14}$$

where ρ is the fluid density; C_{d} is the drag coefficient; and $b \times h$ is the wetted area of the body projected on the plane normal to the flow direction (Yeh 2007). The fluid force at a given location can be determined by use of Eq. 14 combined with the values of hu^2 (momentum flux) shown in Fig. 9c. A complete discussion of tsunami forces acting on structures can be found elsewhere (Yeh 2007). From Fig. 8 it can be gleaned that the water entering the city is stopped by the road

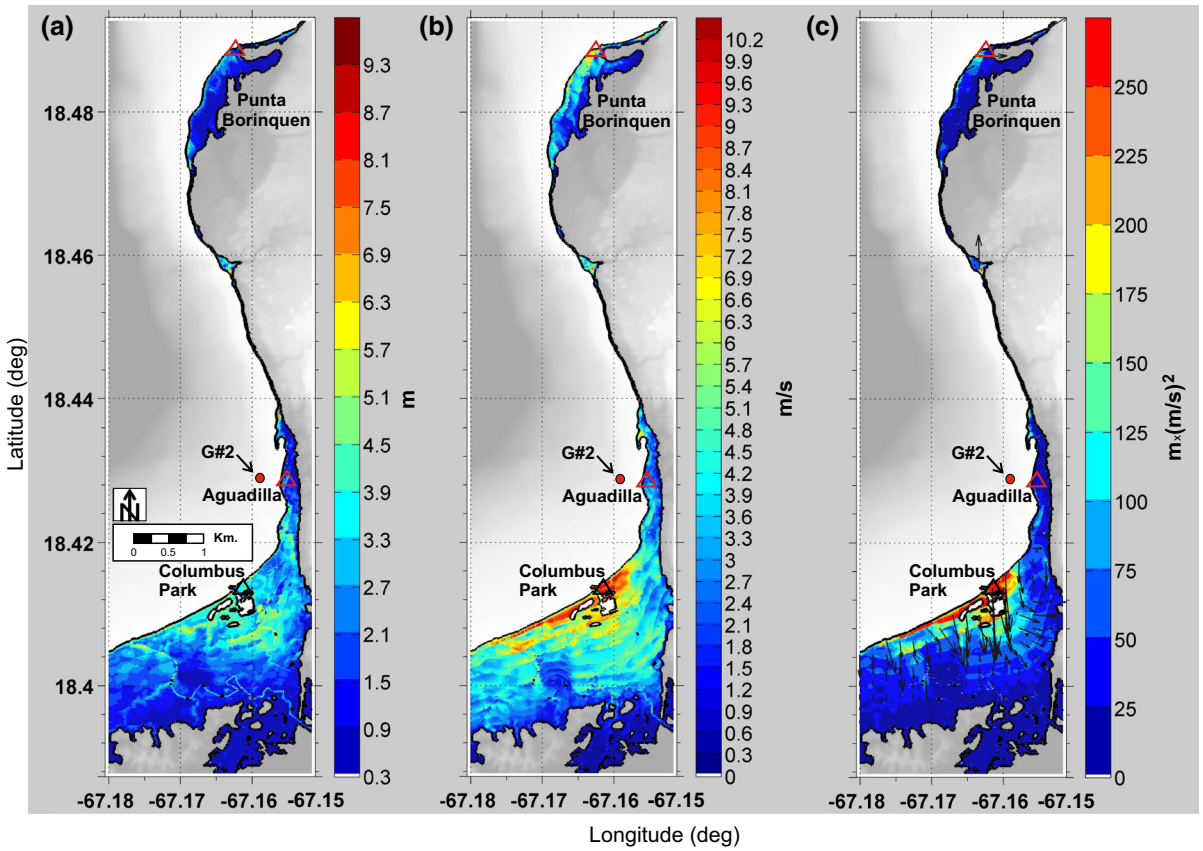

Figure 9
Numerical results in Aguadilla computed on the innermost grid (1/3 arc-second resolution) of the nested grid domain. **a** Inundation depth at maximum momentum flux. **b** Water velocity at maximum momentum flux. **c** Maximum momentum flux values

embankment structure which acts as an inundation protection system. Overall, the momentum flux in the populated area of Aguadilla ranges from 25 to 125 m $\times$ $(\text{m/s})^2$ per unit mass and per unit breadth.

These quantities can be useful for estimation of flow forces on a structure according to its location in the inundation area. For example, in 1893, a monument to commemorate the 400th anniversary of Christopher Columbus landing in Puerto Rico was erected south of the former mouth of the Culebrinas River, the boundary between the town of Aguadilla ($\sim$2 km due northeast) and Aguada. The "Cross of Columbus", also called the "Columbus Monument", consists of a $\sim$10 m^3 base supporting a pillar of $\sim$2.4 m^3 plus a stack of several granite blocks with square sections forming a column ($\sim$2.35 m^3) which supports the capstone cross ($\sim$0.75 m^3). The total height of the monument may have reached 10 m and may have stood up to 100 m from the shore. According to Reid and Taber (1919), the monument, except for its massive base, collapsed during the earthquake, and in turn, tsunami waves carried the monument blocks to distances between 45 and 75 m inland. In 1923, an exact replica of the monument was built using the original base, therefore aiding assessment of the tsunami forces that may have affected the piercing structure during the tsunami. By means of the information obtained from Fig. 9, it is possible to obtain an approximate estimate of the force and overturning moment that might have affected the pillar of the Columbus monument under the tsunami load, where $h = 3.9$ m and $u = 8.1$ m/s are obtained from the color scale at Columbus Park (lower triangle in Fig. 9). The assessment is performed by assuming the pillar survived the earthquake and was destroyed later by the tsunami

flow load. The pillar has a cross section of $\sim 1.2 \times 1.2$ m^2 and stands on the base 1.2 m above the ground, therefore the pillar has an effective flow height of $h = 3.9 - 1.2 = 2.7$ m. Now, considering a steady flow at maximum momentum flux, because tsunamis have a long period, Eq. 14 can be applied. Following the work of Yeh (2007), a drag coefficient of 2 ($C_d = 2$) was used in the calculation. At the base of the piercing structure we thus obtain a shear force of ~ 213 kN and an overturning moment of ~ 288 kN m. The restoring moment owing to the weight of the granite monument ($\rho_{granite} = 2{,}750$ kg/m^3) partially submerged during the tsunami load is ~ 115 kN m which is much less than the overturning moment.

6. Conclusions

In this study we present an improved numerical simulation for the October 11, 1918, tsunami observed along the northwestern coast of Puerto Rico. The work and simulations presented here are based on the assumption that this tsunami was generated by a massive submarine landslide initiated by the earthquake. This study builds on previous research of this event by using an advanced computational system for submarine landslides, in which a well-established and validated 3D–2D coupled model is presented and applied, yielding results comparable with observations. For the 3D phase, the Navier–Stokes model TSUNAMI3D for two fluids (water and landslide material) was used to determine the initial wave characteristic generated by the submarine landslide. To solve for coastal inundation, i.e., wave propagation and detailed runup, the 2D non-hydrostatic numerical model NEOWAVE was used. The 3D model provides the wave kinematics and the free surface configuration for the initial tsunami wave source, which were then input as the initial condition (hot start) to the more numerically efficient 2D model.

The full-scale 3D numerical simulation used a wasting volume of ~ 12.5 km^3 to generate the initial tsunami wave. A wave ~ 48 m high (crest to trough) was recorded 3 min after slide initiation. The outgoing northward positive wave with amplitude of ~ 18 m was followed by a landward negative wave or initial surface depression of ~ 30 m. Shortly after, a rebounding wave emerged from the surface depression between the outgoing and negative backgoing waves, although this rebounding wave did not evolve as a massive wave, but as a short and dispersive wave. The negative wave reached the coastline facing Aguadilla approximately 5 min after initiation of the landslide. These estimates are consistent with the observations of a leading depression and arrival times collected from witnesses. Although the landslide main motion is directed toward the north, a fraction of the tsunami energy is refracted around the Puerto Rico's northwest shelf, apparently affecting the north coastline. A subsequent publication will address this question and the impact along the northern coast of Puerto Rico.

Analysis of the potential and kinetic energy of the system showed that the energy of the wave is largely affected by the landslide motion in the generation region, and this energy is mainly concentrated within the wave-generation area and at depth near the surface of the landslide. Once the initial wave begins to propagate from the generation area, its potential and kinetic energy begin to stabilize. Because the energy outside the generation area is what is propagated toward the shore, and is therefore of importance for inundation and hazard studies, the stabilization of the wave energy in this region indicates the appropriate time to transfer the wave kinematics and free surface information from the full 3D model to the 2D model for detailed inundation calculation.

By using two-way nested grids of 1 and 1/3 arcsecond with the 2D numerical code NEOWAVE, details of the tsunami runup, i.e., sea-level elevation (runup), water depth (inundation), and maximum momentum flux, were obtained for Aguadilla. Figure 8 shows the extent of tsunami inundation in present-day Aguadilla, assuming a hypothetical tsunami if the Mona landslide were to occur today. The expected maximum water elevation in the populated area of Aguadilla ranges from 3 to 9 m with maximum inundation depth from 0.30 to ~ 6.0 m, respectively.

Numerical calculation showed that the water entering the city is stopped by the road embankment structure that acts as an inundation protection system.

The momentum flux in the populated area of Aguadilla ranges from 25 to 125 m $\times$ $(m/s)^2$ per unit mass and per unit breadth. Momentum flux values are important for engineering design purposes or re-assessment of existing structures to verify their capability to resist tsunami loads. The data can also assist coastal managers assessing the vulnerability of infrastructure by identifying the nature and location of major tsunami flows.

Acknowledgments

This study was funded through the National Tsunami Hazards and Mitigation Program (NTHMP) awarded to the Puerto Rico Seismic Network tsunami component. Numerical calibration of the 3D numerical model was, in part, supported by the National Science Foundation (NSF) through the NSF-NEESR award CMMI-0936603. The authors are grateful for valuable help from Harry Justiniano and José Benítez from the Physical Oceanography Laboratory at the Marine Sciences Department—UPRM, IT staff from PRSN, and Uri ten Brink and Jason Chaytor from the Woods Hole Science Center, USGS. Special thanks go to anonymous reviewers, whose comments and suggestions significantly contributed to improvement and the quality of the manuscript.

References

Abadie, S.M., Harris, J.C., Grilli, S.T., Fabre, R., 2012. *Numerical modeling of tsunami waves generated by the flank collapse of the Cumbre Vieja Volcano (La Palma, Canary Islands): Tsunami source and near field effects*. J. Geophys. Res. *117*, C05030.

Campbell, C.S., Cleary, P.W., Hopkins, M., 1995. *Large-scale landslide simulations: Global deformation, velocities and basal friction*. J. Geophys. Res. *100*(B5), 8267–8283.

Casulli, V., Stelling, G.S., 1998. *Numerical simulation of 3D quasihydrostatic, free-surface flows*. J. Hydr. Eng. *124*, 678–686.

Chaytor, J., ten Brink, U.S., 2007. Two-stage Extensional Opening of the Mona Passage as Revealed by New Multibeam Bathymetry and Seismic Reflection Data. Eos Trans. AGU, 88(52), Fall Meeting Suppl., Abstract T13C–1475.

Chaytor, J., ten Brink, U.S., 2010. *Extension in Mona Passage, Northeast Caribbean*. Tectonophysics, *493*, 74–92.

Doser, D.I., Rodríguez, C.M., Flores, C., 2005. Historical earthquakes of the Puerto Rico-Virgin Islands region (1915–1963), in: Mann, P. (Ed.), Active tectonics and seismic hazards of Puerto Rico, the Virgin Islands, and offshore areas. The Geological Society of America. Special Paper 385, pp. 103–114.

Dunbar, P.K., Weaver, C.S., 2008. U.S. States and Territories National Tsunami Hazard Assessment: Historic Record and Sources for Waves. Technical Report Report to National Tsunami Hazard Mitigation Program. NGDC, USGS.

Fritz, H., Hager, W.H., Minor, H.E., 2004. N*ear field characteristic of landslide generated impulsive waves*. J. Wtrwy. Port Coast. and Oc. Eng. ASCE *130*(6), 287–302, doi:10.1061/(ASCE)0733-950X(2004).

Grilli, S.T., Watts, P., 2005. *Tsunami generation by submarine mass failure part I: modeling, experimental validation, and sensitivity analyses*. J. Wtrwy. Port Coast. and Oc. Eng. ASCE *131*(6), 283–297.

Haugen, K.B., Lovholt, F., Harbitz, C.B., 2005. *Fundamental mechanisms for tsunami generation by submarine mass flows in idealized geometries*. Mar. Pet. Geol. *22*, 209–217.

Hirt, C.W., Nichols, B.D., 1981. *Volume of fluid method for the dynamics of free boundaries*. J. Comp. Phys. *39*, 201–225.

Hornbach, M.J., Mondziel, S.A., Grindlay N.R., Frohlich C., Mann P., 2008. D*id a submarine slide trigger the 1918 Puerto Rico tsunami?* Science of Tsunami Hazards, *27*, No. 2, 22–31.

Horrillo, J., 2006. Numerical Method for Tsunami calculations using Full /Navier–Stokes equations and the Volume of Fluid method. Ph.D. thesis. University of Fairbanks.

Horrillo, J., Wood A., Kim, G.-B., A. Parambath A., 2013. *A simplified 3-D /Navier–Stokes numerical model for landslide-tsunami: Application to the Gulf of Mexico*. J. Geophys. Res. Oceans, *118*, 6934–6950, doi:10.1002/2012JC008689.

Kowalik, Z., 2008. *Energy flux as a tool in locating tsunami secondary sources*. Science of Tsunami Hazards, *27*, No. 3, 1–29.

López-Venegas, A.M., ten Brink, U.S., Geist, E., 2008. *Submarine landslide as the source for the October 11, 1918 Mona Passage tsunami: Observations and modeling*. Marine Geology, *254*, 35–46.

Lynett, P., Liu, P.L., 2002. *A numerical study of submarine landslide generated waves and runup*. Proc. Royal Society of London A. *458*, 2885–2910.

Mercado, A., McCann, W., 1998. *Numerical simulation of the 1918 Puerto Rico tsunami*. Natural Hazards, *18*, 57–76.

NTHMP, 2012. National Tsunami Hazard Mitigation Program, in: Proceedings and Results of the 2011 NTHMP Model Benchmarking Workshop; NOAA Special Report, Boulder: U.S. Department of Commerce/NOAA/NTHMP. p. 436.

Reid, H.F., Taber, S., 1919. *The Porto Rico earthquakes of October–November, 1918*. Bull. Seismol. Soc. Am. *9*, 95–127.

Sue, L. P., Nokes, R. I., Walters, R. A., 2006. *Experimental modeling of tsunami generated by underwater landslides*. Science of Tsunami Hazards, *24*, No. 4, 267–287.

Synolakis, C.E., Bernard, E.N., Titov, V.V., Kanoglu, U., Gonzalez, F.I., 2007. OAR PMEL-135 Standards, criteria, and procedures for NOAA evaluation of tsunami numerical models. Technical Report NOAA Tech. Memo. OAR PMEL-135. NOAA/Pacific Marine Environmental Laboratory, Seattle, WA.

ten Brink, U., Danforth, W., Polloni, C., Andrews, B., Llanes, P., Smith, S., Parker, E., Uozumi, T., 2004. *New seafloor map of the Puerto Rico Trench helps assess earthquake and tsunami hazards*. Eos Trans. AGU, *85*, 349,354.

ten Brink, U., Dillon, W., Frankel, A., Rodríguez, R., Mueller, C., 1999. Seismic and tsunami hazard in Puerto Rico and the Virgin Islands. Open-File Report 99–353. U.S. Geological Survey.

TEN BRINK, U.S., GEIST, E., ANDREWS, B.D., 2006. *Size distribution of submarine landslides and its implication to tsunami hazard in Puerto Rico*. Geoph. Res. Lett. *33*, 4.

WATTS, P., 2000. *Tsunami features of solid block underwater landslide*. J. Waterw. Port Coast. Ocean Eng. *126*(3), 144–152.

WATTS, P., GRILLI, S.T., TAPPIN, D.R., FRYER, G.J., 2005. *Tsunami generation by submarine mass failure. part II: Predictive equations and case studies*. J. Waterw. Port Coast. Ocean Eng. *131*(6), 298–310.

YAMAZAKI, Y., KOWALIK, Z., CHEUNG, K.F., 2009. *Depth-integrated, non-hydrostatic model for wave breaking and run-up*. Int. J. Numer. Meth. Fluids, *61*(5), 473–497.

YEH, H., 2007. *Design tsunami forces for onshore structures*. Journal of Disaster Research, *2*, No. 6.

(Received July 11, 2014, revised November 11, 2014, accepted November 12, 2014)